



Boosting photocatalytic cross-dehydrogenative coupling reaction by incorporating $[\text{Ru}^{\text{II}}(\text{bpy})_3]$ into a radical metal-organic framework

Yan-Xi Tan^{a,1}, Shao-Xia Lin^{a,1}, Caiping Liu^a, Yiyin Huang^a, Mi Zhou^{a,b}, Qiang Kang^{a,*}, Daqiang Yuan^{a,*}, Maochun Hong^a

^a State Key Laboratory of Structure Chemistry, Fujian Institute of Research on the Structure of Matter, Chinese Academy of Sciences, Fuzhou, 350002 Fujian, China

^b University of Chinese Academy of Sciences, Beijing, 100049, China



ARTICLE INFO

Keywords:

Metal-organic framework
Triphenylamine-based radical
Photoinduced electron transfer
Heterogeneous catalyst
Mannich photocatalysis

ABSTRACT

Due to energy-efficient and green processes of photocatalysis, the visible-light-driven photocatalytic organic synthesis has developed greatly in the last decade. The well-known photocatalysts, Ru^{II} -polypyridyl complexes, have been extensively exploited in the synthesis of various chemicals. However, homogeneity of Ru^{II} -polypyridyl complexes makes their recycling difficult. Here, we show an effective strategy for boosting photocatalysis by incorporating $[\text{Ru}^{\text{II}}(\text{bpy})_3]$ into a radical metal-organic framework (FJI-Y2). Recyclable photocatalyst FJI-Y2 can efficiently catalyze the cross-dehydrogenative coupling reactions of *N*-phenyltetrahydroisoquinoline derivatives with phosphite esters, forming medicinal α -aminoquinoline phosphonates. More importantly, the photocatalytic efficiency of FJI-Y2 is actually higher than its homogeneous counterpart $[\text{Ru}^{\text{II}}(\text{bpy})_3]\text{Cl}_2$, because multiple intermolecular interactions between 1,4,5,8-naphthalenediimide radicals and $[\text{Ru}^{\text{II}}(\text{bpy})_3]$ induce optimal photoinduced electron transfer process to expedite chemical conversion and recycling of catalysts. It is envisioned that MOFs containing radicals can be ideal platforms to incorporate more noble-metal photocatalysts for promoting photocatalysis.

1. Introduction

Benefiting from sunlight as a sustainable energy source, visible-light-driven photocatalysis is thought to be a clean and energy-efficient process for organic synthesis [1–4]. In the past decades, the Ru^{II} -polypyridyl complexes as visible light photocatalysts, such as $[\text{Ru}^{\text{II}}(\text{bpy})_3]$ ($\text{bpy} = 2,2'$ -bipyridine), have been recognized and extensively exploited in the synthesis of various chemicals [5–11]. For example, the typical light-driven aerobic cross-dehydrogenative coupling (CDC) reaction of *N*-phenyltetrahydroisoquinoline derivatives with phosphite esters can be catalyzed by Ru^{II} or Ir^{III} -polypyridyl complexes to form medicinally important α -aminoquinoline phosphonates via single-electron transfer (SET) processes [6,12–15]. However, these homogeneous noble-metal photocatalysts will hinder their recycling and practical applications. In order to improve recyclability and reduce cost of such photocatalysts, it is effective to trap catalytic motifs into porous matrix [16].

Metal-organic frameworks (MOFs), a type of designable crystalline porous materials, can elucidate the interaction between host frameworks and catalytic centers at the atomic level with the help of single-

crystal X-ray diffraction [17–34]. In particular, incorporation of Ru^{II} -polypyridyl complexes as catalytic active sites into MOFs has been proven to be attractive because of the outstanding chemical stability and high crystallinity of the resulting materials. Based on cation exchange or *in situ* synthesis, some MOFs with anionic hosts can support a $[\text{Ru}^{\text{II}}(\text{bpy})_3]$ photoredox catalyst. However, none of these MOFs showed a well-organized $[\text{Ru}^{\text{II}}(\text{bpy})_3]$ photoredox catalyst, which might hinder the mechanism study [19,21,26]. Moreover, almost all of $[\text{Ru}^{\text{II}}(\text{bpy})_3]$ -loaded MOFs show lower catalytic activity than a comparable amount of individual $[\text{Ru}^{\text{II}}(\text{bpy})_3]$ photoredox catalyst, because heterogeneous catalysis is more disadvantageous for mutual contact between catalysts and substrates than homogeneous catalysis and the host framework itself is catalytically inactive [17,18,35]. Thus, optimizing the catalytic activity of $[\text{Ru}^{\text{II}}(\text{bpy})_3]$ photoredox catalyst in a heterogeneous catalytic system remains a challenge, and developing novel photo-induced electron transfer (PET) process during the photocatalytic process is highly desirable.

To address the above problems, the synergistic effect of radical porous host and $[\text{Ru}^{\text{II}}(\text{bpy})_3]$ photocatalyst is an effective strategy to optimal PET process. It has been reported that radicals are critical

* Corresponding authors.

E-mail addresses: kangq@fjirsm.ac.cn (Q. Kang), ydq@fjirsm.ac.cn (D. Yuan).

¹ These authors contributed equally.

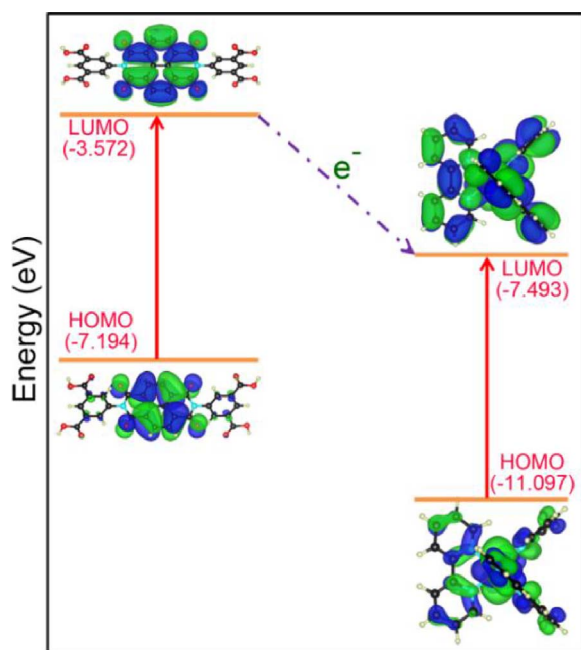


Fig. 1. HOMO-LUMO energy profiles of H₄BINDI (left) and [Ru^{II}(bpy)₃] (right).

intermediates in C–C or C–P bond formation driven by visible light [36–38]. 1,4,5,8-Naphthalenediimide (NDI), which can undergo reversible single-electron reduction to form stable radical anions served as redox-active units, has been considered as an excellent type of organic linker in the construction of photoelectronically active MOFs. However, the photocatalytic properties of the MOFs based on NDI-type organic linkers have been rarely investigated [39–44], which inspires us to explore the synergistic effect of NDI radicals and the [Ru^{II}(bpy)₃] photoredox catalyst in photocatalysis.

We question whether some novel PET pathways between NDI and [Ru^{II}(bpy)₃] photocatalyst will happen through the redox reactions of their excited state? Density functional theory (DFT) calculations were performed on H₄BINDI and [Ru^{II}(bpy)₃] to verify the possibility. DFT calculations (Fig. 1) show that the lowest unoccupied molecular orbital (LUMO) of H₄BINDI fragment (-3.572 eV) lies in higher energy than the LUMO of [Ru^{II}(bpy)₃] (-7.493 eV), indicating the efficient electron transfer may occur from H₄BINDI to [Ru^{II}(bpy)₃] [40,45]. The proposed redox process is also consistent with the redox potentials of key intermediates (i.e., Ru^{II} as oxidant: $E_1 = -1.47\text{ V vs Fc/Fc}^+$; NDI as reductant: $E_2 = -1.83\text{ V vs Fc/Fc}^+$, Fig. S1). Hence, the synergistic effect of NDI radicals and the [Ru^{II}(bpy)₃] photoredox catalyst in visible-light-driven photocatalysis is certainly worth exploring. Moreover, we construct anionic NDI-based MOFs bearing [Ru^{II}(bpy)₃] photoredox catalyst as a charge-balanced cation (Scheme 1) and disclose an unprecedented PET pathway combining NDI radical and [Ru^{II}(bpy)₃] photoredox catalyst.

In this paper, two three-dimensional (3D) porous MOFs, [Mn₃(BINDI)₂(H₂O)Cl] \cdot 3Me₂NH₂ (FJI-Y1, FJI = Fujian Institute, H₄BINDI = N,N'-bis(5-isophthalate acid)naphthalene-diimide) and [Mn₆(BINDI)₄(H₂O)₂Cl₂] \cdot [Ru^{II}(bpy)₃] \cdot 4Me₂NH₂ (FJI-Y2) are

constructed, which have similar Kagomé lattices pillared by NDI groups. For the typical visible-light-driven CDC reactions, the heterogeneous [Ru^{II}(bpy)₃]-loaded FJI-Y2 shows high isolated yield of 80%, which is about 1.43 times enhancement over that of the homogeneous [Ru(bpy)₃]Cl₂. The effective heterogeneous photocatalysis reflects that the multiple intermolecular interactions between [Ru^{II}(bpy)₃] and NDI radicals in the framework induce optimal PET process to expedite chemical conversion and recycling of catalysts.

2. Experimental

2.1. Materials and methods

Commercially available reagents were used as received. Thermal gravimetric analysis data were obtained with a NETZSCH STA 449C analyzer. All samples and reference material (Al₂O₃) were enclosed in a platinum crucible and were heated from 25 °C to 800 °C at a rate of 10 °C/min under N₂ atmosphere. Powder X-ray diffraction (PXRD) patterns were collected on a Rigaku Mini 600 X-ray diffractometer with Cu K α radiation ($\lambda = 1.5406\text{ \AA}$) at a scanning rate of 5°/min for 2θ ranging from 4° to 40°. Simulated XRPD patterns were calculated using Mercury from the single-crystal structural models. Routine ¹H NMR spectra were recorded on a Bruker Avance 400 spectrometer (400.1 MHz for ¹H NMR). The deuterated solvents used are indicated in the experimental details. Optically diffuse reflectance spectra were measured at room temperature on a Perkin Elmer Lambda-950 UV/Vis/NIR spectrophotometer. EPR spectra were recorded on a Bruker BioSpin E500 EPR spectrometer equipped with a 16 mW ultraviolet lamp and using a 100 kHz magnetic field modulation at room temperature. Electrochemical measurements are performed by CV (cyclic voltammetry) CHI760. Elemental mapping analysis was conducted by using a SU-8010 scanning electron microscope.

2.1.1. Preparation of [Mn₃Cl(BINDI)₂(H₂O)] \cdot 3Me₂NH₂*x*guest (FJI-Y1)

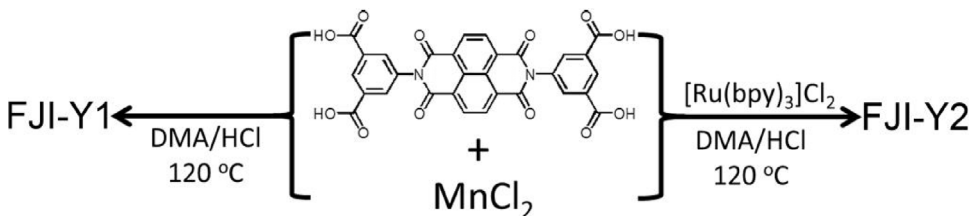
0.05 mmol H₄BINDI (30 mg), 0.25 mmol MnCl₂ \cdot 4H₂O (57 mg), 0.2 ml 4 M HCl and 4 ml DMA were sealed and dissolved in an 8 ml vial, and then heated in an oven at 120 °C for 72 h. The vial was then allowed to cool to room temperature. After washing with fresh DMA, orange crystals were obtained (Yield: 36 mg, 68%, based on H₄BINDI).

2.1.2. Preparation of [Mn₆(BINDI)₄(H₂O)₂Cl₂] \cdot [Ru^{II}(bpy)₃] \cdot 4Me₂NH₂*x*guest (FJI-Y2)

0.05 mmol H₄BINDI (30 mg), 0.25 mmol MnCl₂ \cdot 4H₂O (57 mg), 0.02 mmol [Ru(bpy)₃]Cl₂ (15 mg), 0.2 ml 4 M HCl and 4 ml DMA were sealed in an 8 ml vial and heated in an oven at 120 °C for 72 h. Then the vial was allowed to cool to room temperature. After washing with fresh DMA, red crystals were obtained (Yield: 39 mg, 66%, based on H₄BINDI).

2.2. X-ray crystallography

Diffraction data of FJI-Y1 and FJI-Y2 were collected on a SuperNova diffractometer equipped with a copper micro-focus X-ray source ($\lambda = 1.5406\text{ \AA}$) and an Atlas CCD detector. The structure was solved by direct methods and refined with full-matrix least-squares technique using SHELXL-2016 [46]. All non-hydrogen atoms were refined with anisotropic



Scheme 1. Synthesis of FJI-Y1 (left) and FJI-Y2 (right) by using H₄BINDI ligand and MnCl₂ in the absence and presence of [Ru(bpy)₃]Cl₂, respectively.

displacement parameters. The diffuse electron densities resulting from residual solvent molecules were removed from the dataset using the SQUEEZE routine of PLATON and the data generated were refined further [47]. The contents of the solvent region are not represented in the unit cell contents in the crystal data. **Crystal data of FJI-Y1:** $C_{70}H_{53}N_8O_{26}ClMn_3$ ($M_r = 1622.47$): monoclinic, space group $P2_1/c$, $a = 18.6552(3)$ Å, $b = 21.15630(10)$ Å, $c = 33.4582(5)$ Å, $\beta = 127.765(2)^\circ$, $V = 10439.0(3)$ Å 3 , $Z = 4$, $T = 100.0(5)$ K, $\mu = 3.665$ mm $^{-1}$, $D_{\text{calc}} = 1.032$ g/cm 3 , 190816 reflections measured ($6.684^\circ \leq 2\theta \leq 146.81^\circ$), 20808 unique ($R_{\text{int}} = 0.0503$, $R_{\text{sigma}} = 0.0230$) which were used in all calculations. The final R_1 was 0.0754 ($I > 2\sigma(I)$) and wR_2 was 0.2238 (based on all data). **Crystal data of FJI-Y2:** $C_{154}H_{80}N_{17}O_{50}Cl_2Mn_6Ru$ ($M_r = 3455.95$): monoclinic, space group $P2_1/c$, $a = 31.4652(7)$ Å, $b = 21.1868(6)$ Å, $c = 33.7591(6)$ Å, $\beta = 109.053(2)^\circ$, $V = 21272.5(9)$ Å 3 , $Z = 4$, $T = 100.1(2)$ K, $\mu = 4.164$ mm $^{-1}$, $D_{\text{calc}} = 1.079$ g/cm 3 , 69919 reflections measured ($6.796^\circ \leq 2\theta \leq 142.252^\circ$), 38953 unique ($R_{\text{int}} = 0.0482$, $R_{\text{sigma}} = 0.0675$) which were used in all calculations. The final R_1 was 0.1024 ($I > 2\sigma(I)$) and wR_2 was 0.3083 (based on all data).

2.3. Typical experimental procedure for catalysis

Catalyst FJI-Y2 (1.0 mmol% based on $[\text{Ru}^{II}(\text{bpy})_3]$) and the respective substrate (0.2 mmol) in dry MeCN (0.4 ml) were added to a 10 ml Schleck flask. Then phosphite esters (2.0 equiv.) was added with very slowly stirring and the reaction mixture was placed about 10 cm from a 14 W fluorescent lamp. Upon the completion of reaction after 12 h, as monitored by TLC (petroleum ether/EtOAc = 5:1), the crude reaction mixture was purified by flash chromatography on silica gel (silica: 200–300; eluent: petroleum ether/EtOAc (3:1–2:1) to provide the pure product.

2.4. Electrochemical measurements

The redox potentials of the H_4BINDI and $[\text{Ru}(\text{bpy})_3]\text{Cl}_2$ were measured using a three-electrode cell at room temperature. A platinum electrode was used as the working electrode, platinum wire as the

counter electrode, and a platinum wire as the reference. Electrochemical measurements of the analytes were carried out using 0.01 mmol solutions of tetrabutylammonium hexafluorophosphate solution in acetonitrile. The powdered materials were coated on 3 mm wide platinum electrode. The reduction potentials of the compounds were obtained from the cyclic voltammograms and corrected with respect to the Fc/Fc^+ internal standard.

2.5. Molecular simulations and DFT calculations

To quantitatively evaluate the interactions between BINDI ligands and $[\text{Ru}^{II}(\text{bpy})_3]$ cations, their electronic properties were calculated using DFT. All molecules were optimized using the B3PW912 hybrid functional with 6-31G(d) basis set. The HOMO and LUMO energy levels of BINDI ligand and $[\text{Ru}^{II}(\text{bpy})_3]$ cation were calculated using the B3PW91 hybrid function with 6-311G** basis set. The B3PW91 function was developed by Becke [48] and demonstrated to be computationally accurate and fast for bandgap calculations [49]. All the calculations were carried out using Gaussian 09.

3. Results and discussion

3.1. Crystal structure

Orange single crystals of FJI-Y1, formulated as $[\text{Mn}_3\text{Cl}(\text{BINDI})_2(\text{H}_2\text{O})]\cdot 3\text{Me}_2\text{NH}_2\text{-xguest}$, are obtained by a solvothermal reaction of MnCl_2 , H_4BINDI in *N,N'*-dimethylacetamide (DMA) at 120 °C for 72 h. Single-crystal X-ray diffraction reveals that compound FJI-Y1 crystallizes in the monoclinic space group $P2_1/c$. One prominent structural feature in FJI-Y1 is the presence of Kagomé lattices, whose formation is closely related to two types of building units (Fig. 2a and Fig. S2). One is the extraordinary anionic $[\text{Mn}_2(\text{COO})_4\text{Cl}_2]^{2-}$ paddle-wheel unit (SBU1) with two square-pyramidal Mn^{II} ions bonded by four carboxyl groups and two terminal Cl^- ligands. In the second anionic unit $[\text{Mn}_2(\text{COO})_6(\text{H}_2\text{O})]^-$ (SBU2), one Mn^{II} cation is surrounded by five O atoms from four carboxyl groups to complete the square-pyramidal

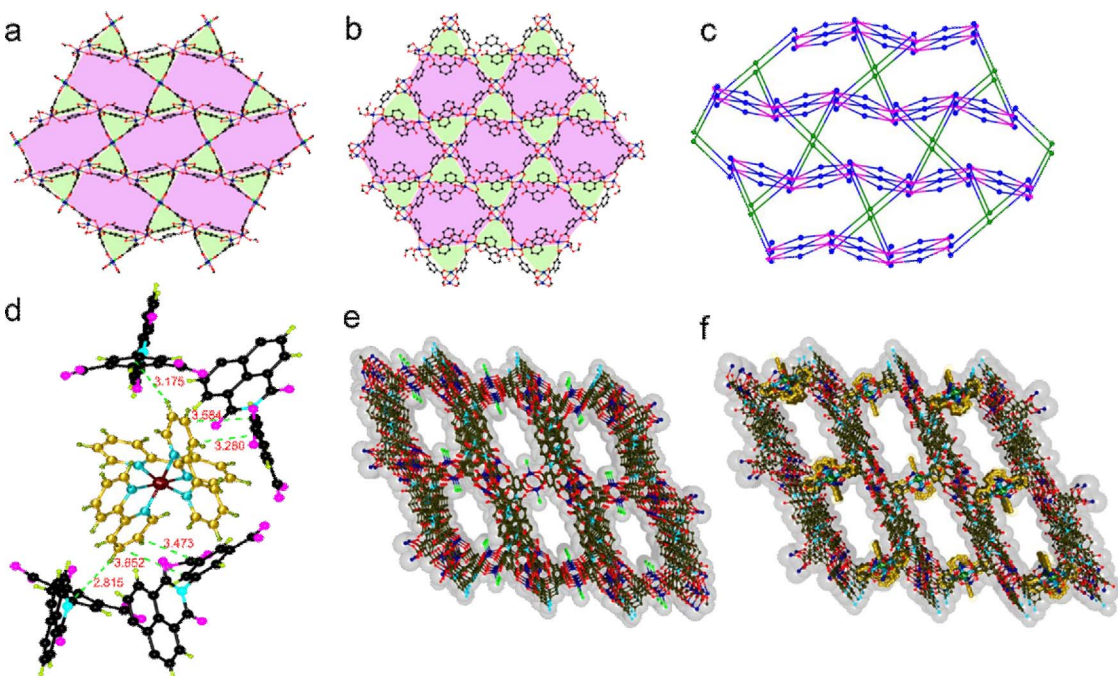


Fig. 2. Structural representations of FJI-Y1 and FJI-Y2. Kagomé lattices in (a) FJI-Y1 and (b) FJI-Y2. (c) (4,6)-connected net in FJI-Y1 and FJI-Y2. (d) Multiple intermolecular interactions between BINDI ligands and $[\text{Ru}^{II}(\text{bpy})_3]$ cations in FJI-Y2. 3D porous frameworks of (e) FJI-Y1, and (f) FJI-Y2, viewed along the b axis, $[\text{Ru}^{II}(\text{bpy})_3]$ cations encapsulated in pores are highlighted as yellow atoms. Note: all coordinated solvent molecules and dissociative $[\text{Me}_2\text{NH}_2]^+$ cations are omitted for clarity. (For interpretation of the references to colour in this figure legend, the reader is referred to the web version of this article.)

coordination geometry. Meanwhile, the other distorted octahedral Mn^{II} cation is coordinated by four carboxyl O atoms and one terminal H₂O. There are hydrogen bonds with N—H···O lengths of 2.74 Å to 2.94 Å and angles of 156.09° to 174.02° between the O atoms of coordinated H₂O or carboxyl groups and charge-balanced [Me₂NH₂]⁺ cations derived from the decomposition of DMA solvent (Fig. S2). One SBU1 unit and two SBU2 units are connected by four isophthalate sections in BINDI ligands to form a three-membered ring, and four SBU2 units and two SBU1 units are connected by eight isophthalate sections in BINDI ligands to form a six-membered ring. Finally, the connection of these three- and six-membered rings by sharing edges further extends the structure into a two-dimensional layer with Kagomé topology (Fig. 2a) [50]. The edge lengths in the Kagomé lattices are 9.37 Å to 10.83 Å. These Kagomé lattices as super secondary building units are further linked to other two adjacent Kagomé lattices by the remaining NDI groups of BINDI ligands along *a* direction, generating a 3D porous anionic pillar-layer motif with one-dimensional (1D) channels along the *a* and *b* axes (Fig. 2e and Fig. S3). These channels with a window size of about 9 × 11 Å² (atom to atom distance) are filled with disordered solvent molecules and charge-balancing [Me₂NH₂]⁺ cations. Topologically, the framework of FJI-Y1 can be described as a (4,6)-connected net with stoichiometry of (4-c)₅(6-c)₂ by reducing each SBU1 unit, SBU2 unit and BINDI ligand as the 4-, 6- and 4-connected nodes, respectively (Fig. 2c).

Red single crystals of FJI-Y2, formulated as [Mn₆(BINDI)₄(H₂O)₂Cl₂][−]·[Ru^{II}(bpy)₃]⁺·4Me₂NH₂·xguest, are obtained from the similar reaction of FJI-Y1, in the presence of [Ru(bpy)₃]Cl₂. Single-crystal X-ray diffraction reveals that compound FJI-Y2 has similar (4,6)-connected network with Kagomé lattices pillared by NDI section of the BINDI ligands. Interestingly, there are two kinds of charge-balanced cations. One is the common [Me₂NH₂]⁺, and another one is the extraordinary photocatalyst [Ru^{II}(bpy)₃] located in the pores (Fig. S5). Although some MOFs have been reported to capture [Ru^{II}(bpy)₃] cations into their pores by solvent-assisted cation exchange or synthesis *in situ* [19,35,51–55], the distinct structure of [Ru^{II}(bpy)₃] in framework is often hard to determine due to severe disorder and partial occupy. Furthermore, these [Ru^{II}(bpy)₃] cations in FJI-Y2 are considered to be uniform and accessible catalytic centers that enhance catalytic activity by eliminating the deactivation pathways caused by agglomeration of catalyst. These [Ru^{II}(bpy)₃] cations are restricted in the pores by multiple intermolecular interactions, such as short C—H···π lengths of 3.105 Å and 3.142 Å measured as the distance between the H atoms and the phenyl centroids, and slipped π stacking with lengths of 3.297 Å to 3.791 Å measured as the distance between two C atoms from the phenyl rings of BINDI ligands and pyridine rings of [Ru^{II}(bpy)₃] cations (Fig. 2d). In FJI-Y2, the [Mn₂(COO)₆Cl₂]^{2−} paddle-wheel unit is similar to that of FJI-Y1. However, the presence of such large [Ru^{II}(bpy)₃] cations leads to the rotation of BINDI ligands, and further affects the coordination geometries of Mn(II) and BINDI ligands in two

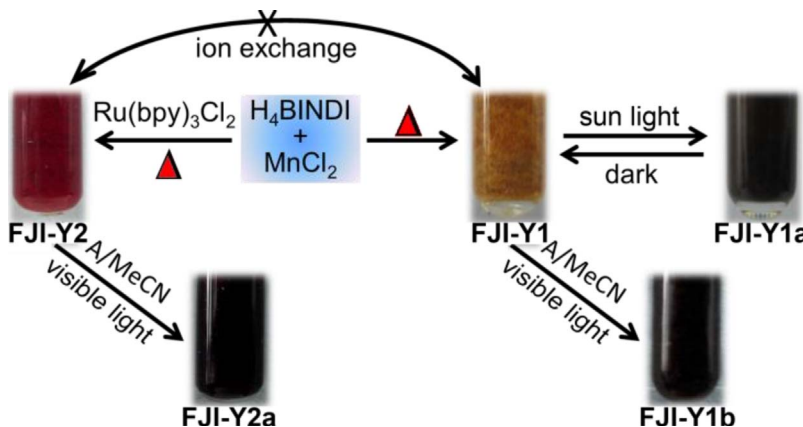
2(COO)₆(H₂O)₂][−]单位 (Fig. S4), 在其中一些氢键与N—H···O长度为2.64 Å到2.83 Å和角度为153.02°到169.19°之间的O原子从羧基集团和[Me₂NH₂]⁺阳离子也可以看到。因此，与FJI-Y1相比，FJI-Y2中的Kagomé晶胞明显扭曲 (Fig. 2b)。尽管FJI-Y2包覆了大的[Ru^{II}(bpy)₃]阳离子，但FJI-Y2的结构生成了1D通道，窗口大小约为8 × 12 Å² (原子到原子距离) 沿***b***轴 (Fig. 2f)。

合成的样品都是晶体颗粒，不是粉末。为了进一步证实其纯度，将湿晶体磨碎并用于粉末X射线衍射(PXRD)测量。与模拟的PXRD模式相比，存在一些额外的弱峰归因于溶剂在孔隙和表面引起的背景。为了促进催化，高孔隙率和开放通道对于高效运输底物和产物分子至关重要。然而，预期的Brunauer-Emmett-Teller(BET)表面积无法通过N₂吸附测量支持，因为框架在去除溶剂后会塌陷，这是许多多孔MOFs的常见现象。尽管如此，FJI-Y1和FJI-Y2在DMA和MeCN中的稳定性(Figs. S7和S8)表明它们在光催化方面的稳定性。为了更好地理解孔隙结构，其孔隙参数使用Zeo++软件进行估计。[56] FJI-Y1和FJI-Y2的可及体积分别为43.3%和38.2%，根据理论孔隙体积0.44和0.36 cm³/g，分别计算得出。它们的估计表面积为1455和1210 m²/g，分别。FJI-Y2的模拟孔径分布(PSD)显示了主导的微孔分布，尺寸在8.3–9.7 Å之间，类似于FJI-Y1(Fig. S9)。

3.2. Optical property

如图3所示，FJI-Y1在空气中稳定，在阳光下由橙色变为深绿色(FJI-Y1a)，并在黑暗中恢复为橙色。在MeCN溶液中，FJI-Y1在可见光照射下变为另一种深绿色材料(FJI-Y1b)。PXRD显示FJI-Y1a和FJI-Y1b的晶体结构与FJI-Y1相同。NDI单元已知具有氧化活性，可以在光照射下产生自由基。这种光响应行为可能源于无结构性质的光诱导电子转移化学过程 [40]。如图4c所示，FJI-Y1的UV/Vis光谱显示在390 nm处有强吸收带，对应于n-π*和π-π*跃迁。

Fig. 3. Light induced photochromism of FJI-Y1 and FJI-Y2 under the irradiation of visible light. (A = *N*-phenyltetrahydroisoquinoline).



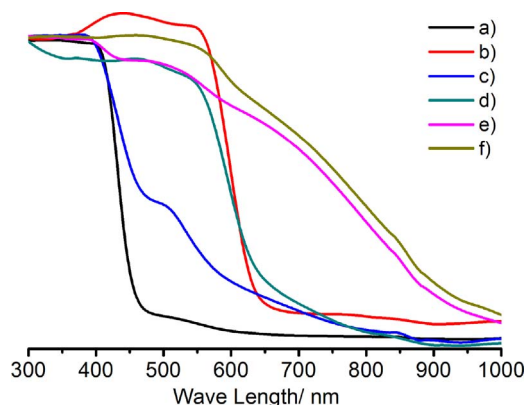


Fig. 4. Solid state UV-vis spectra. (a) H_4BINDI , (b) $[\text{Ru}^{\text{II}}(\text{bpy})_3]\text{Cl}_2$, (c) **FJI-Y1**, (d) **FJI-Y2**, (e) **FJI-Y1b**, (f) **FJI-Y2a**.

BINDI ligands [39,40], and which can also be seen in the UV/Vis spectrum of H_4BINDI ligands (Fig. 4a). The band gap energy of **FJI-Y1** is 2.24 eV calculated from UV-vis data. However, the UV-vis spectrum of **FJI-Y1b** shows an abrupt change in absorption band which reveals that reversible photochromism may result from a photo-induced electron-transfer chemical process inside the structure (Fig. 4e) [36,37,40], giving its band-gap energy of 1.25 eV (Fig. 4e). The spectrum of **FJI-Y2** displays a transformation of the shoulder peak at 501 nm, into a broad band in the region of 510–830 nm, which is similar to that of photocatalyst $[\text{Ru}(\text{bpy})_3]\text{Cl}_2$ (Fig. 4b and d). The band-gap energy of **FJI-Y2**, calculated from UV-vis data is 1.86 eV. After being immersed in a solution of A in MeCN and irradiated with visible light, red **FJI-Y2** can also turn into another dark red species (**FJI-Y2a**) without structural transformation, as confirmed by PXRD measurements (Figs. 3 and S8). Compared to **FJI-Y2**, the absorption edge of **FJI-Y2a** is red shifted and the band-gap energy is reduced to 1.24 eV because of the photo-responsive behaviour resulting from an electron-transfer chemical process between the $[\text{Ru}^{\text{II}}(\text{bpy})_3]$ cations and BINDI ligands (Fig. 4f).

3.3. CDC reaction of *N*-phenyltetrahydroisoquinoline (A) with phosphite esters (B)

Based on the above results, we become interested in the development of a novel SET pathway between NDI radicals and $[\text{Ru}^{\text{II}}(\text{bpy})_3]$ photocatalysts by using the typical CDC reaction of *N*-phenyltetrahydroisoquinoline (A) with phosphite esters (B) as a probe reaction. This will demonstrate the utility and applicability of photoredox catalysis in organic chemistry. As shown in Table 1, the controlled experiments indicate that light, oxygen and the MOF photocatalyst are all necessary for such typical CDC reaction (Entries 1, 3, 6 and 7; Table 1). Employing **FJI-Y1** as catalyst (Entry 4; Table 1), the reaction affords desired product α -aminophosphonate (C) with an isolated yield of 7% after 12 h. This yield is much lower than that (56%) of homogeneous 1 mmol% $[\text{Ru}(\text{bpy})_3]\text{Cl}_2$ catalyst (Entry 2; Table 1). For **FJI-Y2** (1 mmol% based on $[\text{Ru}^{\text{II}}(\text{bpy})_3]$), the isolated yield of the reaction after 12 h is up to 80% (Entry 8; Table 1), which is much higher than that produced by 1 mmol% $[\text{Ru}(\text{bpy})_3]\text{Cl}_2$ as homogeneous catalyst, and also higher than that (62%, Entry 5; Table 1) of mixed catalysts of $[\text{Ru}(\text{bpy})_3]\text{Cl}_2$ and **FJI-Y1**. This is an extraordinary phenomenon for a photocatalytic process catalyzed by MOFs. Although some $[\text{Ru}^{\text{II}}(\text{bpy})_3]$ -loading MOFs were employed as photocatalysts in aerobic oxidative reactions, most of them showed lower catalytic activity than a comparable amount of individual $[\text{Ru}(\text{bpy})_3]\text{Cl}_2$ photoredox catalyst due to the untoward contact between catalyst and substrates in heterogeneous catalysis and the absence of PET between porous host and $[\text{Ru}^{\text{II}}(\text{bpy})_3]$. For catalyst **FJI-Y2**, the multiple intermolecular interactions between $[\text{Ru}^{\text{II}}(\text{bpy})_3]$ cations and BINDI ligands with NDI radicals are conducive

Table 1

The visible light induced aerobic CDC reactions of *N*-phenyltetrahydroisoquinoline (A) with diethyl phosphite (B) catalyzed by different catalysts.^a

Entry	Catalyst	Time/hour	Yield/% ^b
1	None	12	trace
2	$[\text{Ru}(\text{bpy})_3]\text{Cl}_2$	12	56
3 ^c	$[\text{Ru}(\text{bpy})_3]\text{Cl}_2$	12	trace
4	FJI-Y1	12	7
5	$[\text{Ru}(\text{bpy})_3]\text{Cl}_2 + \text{FJI-Y1}$	12	62
6 ^d	FJI-Y2	12	trace
7 ^e	FJI-Y2	12	trace
8	FJI-Y2	12	80
9	FJI-Y2	4	29
10 ^f	FJI-Y2	4 + 8	29

^a Reaction conditions: substrate A (0.2 mmol), diethyl phosphite B (0.4 mmol), catalysts (1 mmol%) in 0.4 ml MeCN exposed to air with visible light irradiation at room temperature.

^b Isolated Yield.

^c The reaction in the presence of $[\text{Ru}(\text{bpy})_3]\text{Cl}_2$ was stirred under the dark and air atmosphere.

^d The reaction in the presence of **FJI-Y2** was stirred under the dark and air atmosphere.

^e The reaction mixture was strictly degassed and then irradiated under an Ar atmosphere.

^f Filtration testing by removing the catalyst **FJI-Y2** after 4 h and continuing the reaction for another 8 h.

to optimal PET process promoting the photocatalytic conversion of chemical bonds in the aerobic CDC reaction. In addition, elemental mapping analysis (Fig. S11) indicates the spatial distribution of well-defined $[\text{Ru}^{\text{II}}(\text{bpy})_3]$ cations in **FJI-Y2** is uniform catalytic centers accessible to enhanced catalytic activity by elimination of the deactivation pathways caused by agglomeration of $[\text{Ru}^{\text{II}}(\text{bpy})_3]$ catalyst [57].

Removal of the catalyst after 4 h (yield: 29%, Entry 9; Table 1) results in no further production C after a further 8 h of irradiation (Entry 10; Table 1), indicating the heterogeneous nature of catalyst **FJI-Y2**. The reusability of the catalyst **FJI-Y2** is then investigated as shown in Table 2. The same batch of catalyst **FJI-Y2** is used over three successive catalytic cycles. The results indicate that the catalytic efficiency of **FJI-Y2** is no significant loss after three cycles. In addition, PXRD measurements of the recycled **FJI-Y2** reveal maintenance of its crystalline structure and framework, confirming the stability of framework in the catalytic system (Fig. S8).

To investigate the generality of this aerobic CDC reaction catalyzed by **FJI-Y2**, the substrate scope is examined and the results are shown in

Table 2

The visible light induced aerobic CDC reactions of *N*-phenyltetrahydroisoquinoline derivatives (A) with phosphite esters (B) catalyzed by catalyst **FJI-Y2**.^a

Entry	$-\text{R}_1$ and $-\text{R}_2$	Yield/% ^b
1	-H and -Me	82/81/78
2	-Me and -Me	78/76/75
3	-OMe and -Me	84/82/82
4	-Br and -Me	89/88/87
5	-H and -Et	80/78/76/75/71 ^c
6	-Me and -Et	77/75/73
7	-OMe and -Et	85/83/75
8	-Br and -Et	86/85/85
9	-H and i-Pr	69/67/67
10	-Me and i-Pr	62/61/61
11	-OMe and i-Pr	66/65/66

^a Reaction conditions: substrate A (0.2 mmol), phosphite esters B (0.4 mmol), catalyst **FJI-Y2** (1 mmol% based on $[\text{Ru}^{\text{II}}(\text{bpy})_3]$) in 0.4 ml MeCN exposed to air with visible light irradiation at room temperature for 12 h.

^b Isolated yields for the first three runs.

^c Five cycles have been done.

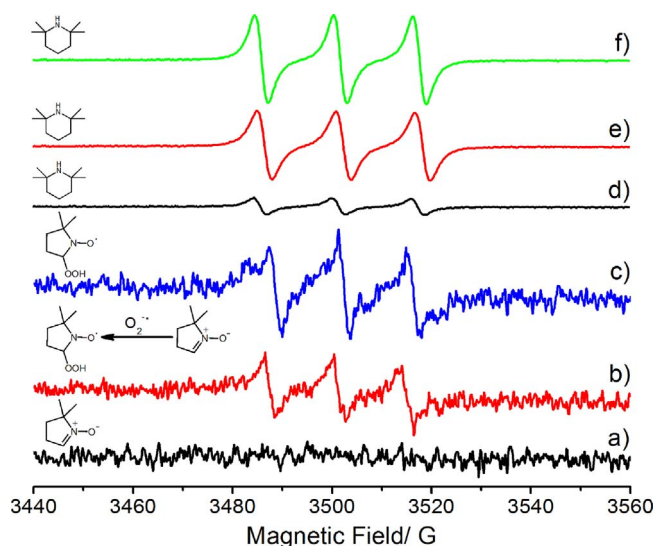
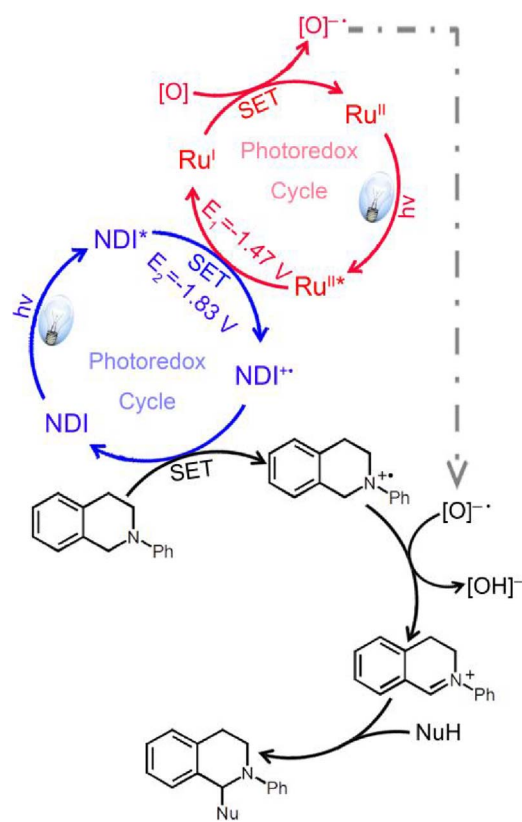


Fig. 5. EPR spectra of CH_3CN solution with DMPO (a); with FJI-Y2 and DMPO (b); with FJI-Y2, A and DMPO (c) under irradiation of visible light for 60 min. EPR spectra of CH_3CN solution with TEMP (d); with FJI-Y2 and TEMP (e); with FJI-Y2, A and TEMP (f) under irradiation of visible light for 60 min.

Table 2. It can be observed that various substituted tetrahydroisoquinoline derivatives can undergo aerobic CDC reactions with diethyl phosphite, catalyzed by FJI-Y2 under visible light, giving the coupling products in good to excellent yields and showing reservation of the catalytic activity after three cycles (Entries 5–8; Table 2). It is also observed that various substituted tetrahydroisoquinolines can undergo aerobic CDC reactions with smaller dimethyl phosphite (Entries 1–4; Table 2) and bigger isopropyl phosphite (Entries 9–11; Table 2) catalyzed by photocatalyst FJI-Y2 under visible light. As the sizes of substituent groups in phosphite esters increase, the yields decrease because large substituent groups hinder the contact between two substrates.

To understand the photocatalytic process of FJI-Y2 in detail, the electron paramagnetic resonance (EPR) spectroscopy measurements are conducted in 5,5-dimethyl-1-pyrroline-N-oxide (DMPO) and 2,2,6,6-tetramethylpiperidine (TEMP) for capture of superoxide radical anion $\text{O}_2^{\cdot-}$ and singlet oxygen ${}^1\text{O}_2$, respectively. As shown in Fig. 5, upon irradiation of the CH_3CN mixture of FJI-Y2 and DMPO in air, generated $\text{O}_2^{\cdot-}$ under the reaction condition reacts with DMPO to form final superoxide, which is confirmed by EPR spectroscopy (Fig. 5b). As shown in Fig. 5d–f, no ${}^1\text{O}_2$ can be generated during the photocatalysis process. These findings indicate that $\text{O}_2^{\cdot-}$ is the active intermediate species in the reaction. It is noted that the differences in above peak intensities are mainly caused by the different dose of tested solvent, which is very hard to control by using capillary for sampling.

In an effort to understand the catalytic reaction, we postulate the reaction mechanism shown in Scheme 2. Upon irradiation by visible light, the NDI groups in FJI-Y2 are converted to the excited state NDI*, which is immediately quenched by the visible light excited $[\text{Ru}^{\text{II}}(\text{bpy})_3]$ via a novel SET process to generate a low-valent Ru^{I} complex and the radical cation NDI $^{\cdot+}$. Molecule A transfers an electron to the radical cation NDI $^{\cdot+}$ to form the radical anion A $^{\cdot-}$, and simultaneously reduces NDI $^{\cdot+}$ to its ground state, while the Ru^{I} complex turnover can be accomplished by the reduction of oxygen [O] to the superoxide radical anion [O] $^{\cdot-}$. These [O] $^{\cdot-}$ may abstract a hydrogen atom from the radical cation A $^{\cdot-}$ to form the desired iminium ion. Addition of nucleophile to the iminium ion leads to the desired product. Such novel photoinduced SET process between NDI radical and $[\text{Ru}^{\text{II}}(\text{bpy})_3]$ photocatalyst may be correlative to the multiple intermolecular interactions (such as C–H $\cdots\pi$ and slipped $\pi\cdots\pi$ interactions) between $[\text{Ru}^{\text{II}}(\text{bpy})_3]$ cations and BINDI ligands in the host framework, affording



Scheme 2. Proposed cooperative catalysis mechanism of NDI radical (blue cycle) and $[\text{Ru}^{\text{II}}(\text{bpy})_3]$ photocatalyst (red cycle) via a novel SET pathway. (For interpretation of the references to colour in this figure legend, the reader is referred to the web version of this article.)

optimal electron or energy transfer, expediting the recycling of two photoredox catalysts [52], and further promoting their catalytic activities. Furthermore, individual photocatalytic processes of BINDI ligand and $[\text{Ru}^{\text{II}}(\text{bpy})_3]$ photocatalyst (Schemes S1 and S2) can't be ignored.

4. Conclusions

In summary, we have for the first time combined 1,4,5,8-naphthalenediimide (NDI) radicals and $[\text{Ru}^{\text{II}}(\text{bpy})_3]$ photocatalysts into an anionic MOF, namely $[\text{Mn}_6(\text{BINDI})_4(\text{H}_2\text{O})_2\text{Cl}_2]\cdot[\text{Ru}^{\text{II}}(\text{bpy})_3]\cdot 4\text{Me}_2\text{NH}_2$ (FJI-Y2), which is described as a novel (4,6)-connected net consisted of Kagomé lattices with redox-active NDI groups as pillars. Molecular simulations and DFT calculations indicate that multiple intermolecular interactions (such as C–H $\cdots\pi$ and slipped $\pi\cdots\pi$ interactions) between NDI radicals and photoredox catalysts $[\text{Ru}^{\text{II}}(\text{bpy})_3]$ contribute to optimal photoinduced SET process promoting the photocatalytic conversion of chemical bonds and expediting the recycling of catalysts. Such extraordinary catalytic mechanism has been demonstrated by the typical aerobic CDC reactions of N-phenyltetrahydroisoquinoline and its derivatives with phosphite esters. The catalytic activity of the recycled $[\text{Ru}^{\text{II}}(\text{bpy})_3]$ -loading FJI-Y2 is about 1.43 times enhancement over that of homogeneous photocatalyst $[\text{Ru}(\text{bpy})_3]\text{Cl}_2$, and the best yield of medicinally important α -Aminoquinoline phosphonates can be reached up to 89%. These results indicate that MOFs containing radicals can be ideal platforms to incorporate more noble-metal photocatalysts for promoting photocatalysis.

Acknowledgements

This work was financially supported by “Strategic Priority Research Program” of the Chinese Academy of Sciences (XDB20000000), Key

Research Program of Frontier Sciences of the Chinese Academy of Sciences (QYZDB-SSW-SLH019), the National Nature Science Foundation of China (21390392, 21603229 and 21771177), and the Nature Science Foundation of Fujian Province (2016J01080).

Appendix A. Supplementary data

Supplementary data associated with this article can be found, in the online version, at <https://doi.org/10.1016/j.apcatb.2018.01.048>.

References

- [1] D. Ravelli, D. Dondi, M. Fagnoni, A. Albini, Photocatalysis, a multi-faceted concept for green chemistry, *Chem. Soc. Rev.* 38 (2009) 1999–2011.
- [2] J.C.K. Chu, T. Rovis, Amide-directed photoredox-catalysed CC bond formation at unactivated sp^3 CH bonds, *Nature* 539 (2016) 272–275.
- [3] L. Zeng, X. Guo, C. He, C. Duan, Metal–organic frameworks: versatile materials for heterogeneous photocatalysis, *ACS Catal.* 6 (2016) 7935–7947.
- [4] D.M. Schultz, T.P. Yoon, Solar synthesis prospects in visible light photocatalysis, *Science* 343 (2014).
- [5] J.I. Day, K. Teegardin, J. Weaver, J. Chan, Advances in photocatalysis: a microreview of visible light mediated ruthenium and iridium catalyzed organic transformations, *Org. Process Res. Dev.* 20 (2016) 1156–1163.
- [6] M. Rueping, S. Zhu, R.M. Koenigs, Photoredox catalyzed CP bond forming reactions–visible light mediated oxidative phosphorylations of amines, *Chem. Commun.* 47 (2011) 8679–8681.
- [7] Y.Q. Zou, L.Q. Lu, L.F. Fu, N.J. Chang, J. Rong, J.R. Chen, W.J. Xiao, Visible-light-induced oxidation/[3 + 2] cycloaddition/oxidative aromatization sequence: a photocatalytic strategy to construct pyrrolo[2,1-a]isoquinolines, *Angew. Chem. Int. Ed.* 50 (2011) 7171–7175.
- [8] Y.-Q. Zou, J.-R. Chen, X.-P. Liu, L.-Q. Lu, R.L. Davis, K.A. Jørgensen, W.-J. Xiao, Highly efficient aerobic oxidative hydroxylation of arylboronic acids: photoredox catalysis using visible light, *Angew. Chem. Int. Ed.* 51 (2012) 784–788.
- [9] C.K. Prier, D.A. Rankic, D.W. MacMillan, Visible light photoredox catalysis with transition metal complexes: applications in organic synthesis, *Chem. Rev.* 113 (2013) 5322–5363.
- [10] S. Zhang, L. Li, S. Zhao, Z. Sun, M. Hong, J. Luo, Hierarchical metal–organic framework nanoflowers for effective CO_2 transformation driven by visible light, *J. Mater. Chem. A* 3 (2015) 15764–15768.
- [11] G. Zhang, C. Bian, A. Lei, Advances in visible light-mediated oxidative coupling reactions, *Chin. J. Catal.* 36 (2015) 1428–1439.
- [12] M. Rueping, C. Vila, T. Bootwicha, Continuous flow organocatalytic CH functionalization and cross-dehydrogenative coupling reactions: visible light organophotocatalysis for multicomponent reactions and CC, CP bond formations, *ACS Catal.* 3 (2013) 1676–1680.
- [13] W.-J. Yoo, S. Kobayashi, Efficient visible light-mediated cross-dehydrogenative coupling reactions of tertiary amines catalyzed by a polymer-immobilized iridium-based photocatalyst, *Green Chem.* 16 (2014) 2438–2442.
- [14] K. Ramakrishna, J.M. Thomas, C. Sivasankar, A green approach to the synthesis of α -amino phosphonate in water medium: carbene insertion into the NH bond by Cu (I) catalyst, *J. Org. Chem.* 81 (2016) 9826–9835.
- [15] Z. Yan, B. Wu, X. Gao, M.-W. Chen, Y.-G. Zhou, Enantioselective synthesis of α -amino phosphonates via Pd-catalyzed asymmetric hydrogenation, *Org. Lett.* 18 (2016) 692–695.
- [16] K. Mori, H. Yamashita, Metal complexes supported on solid matrices for visible-light-driven molecular transformations, *Chem. Eur. J.* 22 (2016) 11122–11137.
- [17] C. Wang, Z. Xie, W. Lin, Doping metal–organic frameworks for water oxidation, carbon dioxide reduction, and organic photocatalysis, *J. Am. Chem. Soc.* 133 (2011) 13445–13454.
- [18] J.-L. Wang, C. Wang, K.E. Dekrafft, W. Lin, Cross-linked polymers with exceptionally high Ru(bpy)₃²⁺ loadings for efficient heterogeneous photocatalysis, *ACS Catal.* 2 (2012) 417–424.
- [19] S. Han, Y. Wei, B.A. Grzybowski, A metal–organic framework stabilizes an occluded photocatalyst, *Chem. Eur. J.* 19 (2013) 11194–11198.
- [20] C.A. Kent, D. Liu, A. Ito, T. Zhang, M.K. Brenneman, T.J. Meyer, W. Lin, Rapid energy transfer in non-porous metal–organic frameworks with caged Ru (bpy) 3 2+ chromophores: oxygen trapping and luminescence quenching, *J. Mater. Chem. A* 1 (2013) 14982–14989.
- [21] R.W. Larsen, L. Wojtas, Photoinduced inter-cavity electron transfer between Ru(II)-tris(2,2'-bipyridine) and Co(II)-tris(2,2'-bipyridine) co-encapsulated within a Zn(II)-trimesic acid metal organic framework, *J. Mater. Chem. A* 1 (2013) 14133–14139.
- [22] T. Toyao, M. Saito, S. Dohshi, K. Mochizuki, M. Iwata, H. Higashimura, Y. Horiuchi, M. Matsuoka, Development of a Ru complex-incorporated MOF photocatalyst for hydrogen production under visible-light irradiation, *Chem. Commun.* 50 (2014) 6779–6781.
- [23] X. Yu, S.M. Cohen, Photocatalytic metal–organic frameworks for the aerobic oxidation of arylboronic acids, *Chem. Commun.* 51 (2015) 9880–9883.
- [24] Z.-M. Zhang, T. Zhang, C. Wang, Z. Lin, L.-S. Long, W. Lin, Photosensitizing metal–organic framework enabling visible-light-driven proton reduction by a Wells–Dawson-type polyoxometalate, *J. Am. Chem. Soc.* 137 (2015) 3197–3200.
- [25] X. Lin, F. Luo, L. Zheng, G. Gao, Y. Chi, Fast, sensitive, and selective ion-triggered disassembly and release based on tris(bipyridine)ruthenium(ii)-functionalized metal–organic frameworks, *Anal. Chem.* 87 (2015) 4864–4870.
- [26] X.J. Kong, Z. Lin, Z.M. Zhang, T. Zhang, W. Lin, Hierarchical integration of photosensitizing metal–organic frameworks and nickel-containing polyoxometalates for efficient visible-light-driven hydrogen evolution, *Angew. Chem. Int. Ed.* 55 (2016) 6411–6416.
- [27] H. Liu, J. Zhang, D. Ao, Construction of heterostructured ZnIn₂S₄@NH₂-MIL-125(Ti) nanocomposites for visible-light-driven H₂ production, *Appl. Catal. B* 221 (2018) 433–442.
- [28] Y.-X. Tan, Y.-P. He, D. Yuan, J. Zhang, Use of aligned triphenylamine-based radicals in a porous framework for promoting photocatalysis, *Appl. Catal. B* 221 (2018) 664–669.
- [29] G. Zhou, M.-F. Wu, Q.-J. Xing, F. Li, H. Liu, X.-B. Luo, J.-P. Zou, J.-M. Luo, A.-Q. Zhang, Synthesis and characterizations of metal-free semiconductor/MOFs with good stability and high photocatalytic activity for H₂ evolution: a novel Z-scheme heterostructured photocatalyst formed by covalent bonds, *Appl. Catal. B* 220 (2018) 607–614.
- [30] M. Wen, K. Mori, Y. Kuwahara, T. An, H. Yamashita, Design and architecture of metal organic frameworks for visible light enhanced hydrogen production, *Appl. Catal. B* 218 (2017) 555–569.
- [31] X. Liu, R. Dang, W. Dong, X. Huang, J. Tang, H. Gao, G. Wang, A sandwich-like heterostructure of TiO₂ nanosheets with MIL-100(Fe): a platform for efficient visible-light-driven photocatalysis, *Appl. Catal. B* 209 (2017) 506–513.
- [32] J. Qin, S. Wang, X. Wang, Visible-light reduction CO₂ with dodecahedral zeolitic imidazolate framework ZIF-67 as an efficient co-catalyst, *Appl. Catal. B* 209 (2017) 476–482.
- [33] F. Jing, R. Liang, J. Xiong, R. Chen, S. Zhang, Y. Li, L. Wu, MIL-68(Fe) as an efficient visible-light-driven photocatalyst for the treatment of a simulated waste-water contain Cr(VI) and Malachite Green, *Appl. Catal. B* 206 (2017) 9–15.
- [34] Z. Yang, X. Xu, X. Liang, C. Lei, Y. Cui, W. Wu, Y. Yang, Z. Zhang, Z. Lei, Construction of heterostructured MIL-125/Ag/g-C₃N₄ nanocomposite as an efficient bifunctional visible light photocatalyst for the organic oxidation and reduction reactions, *Appl. Catal. B* 205 (2017) 42–54.
- [35] X. Wang, W. Lu, Z.-Y. Gu, Z. Wei, H.-C. Zhou, Topology-guided design of an anionic bor-network for photocatalytic [Ru(bpy)₃]²⁺ encapsulation, *Chem. Commun.* 52 (2016) 1926–1929.
- [36] X.-Z. Wang, Q.-Y. Meng, J.-J. Zhong, X.-W. Gao, T. Lei, L.-M. Zhao, Z.-J. Li, B. Chen, C.-H. Tung, L.-Z. Wu, The singlet excited state of BODIPY promoted aerobic cross-dehydrogenative-coupling reactions under visible light, *Chem. Commun.* 51 (2015) 11256–11259.
- [37] L. Zeng, T. Liu, C. He, D. Shi, F. Zhang, C. Duan, Organized aggregation makes insoluble perylene diimide efficient for the reduction of aryl halides via consecutive visible light-induced electron-transfer processes, *J. Am. Chem. Soc.* 138 (2016) 3958–3961.
- [38] X. Geng, F. Lin, X. Wang, N. Jiao, Azidofluoroalkylation of alkenes with simple fluoroalkyl iodides enabled by photoredox catalysis, *Org. Lett.* 19 (2017) 4738–4741.
- [39] L. Han, L. Qin, L. Xu, Y. Zhou, J. Sun, X. Zou, A novel photochromic calcium-based metal–organic framework derived from a naphthalene diimide chromophore, *Chem. Commun.* 49 (2013) 406–408.
- [40] A. Mallick, B. Garai, M.A. Addicoat, P.S. Petkov, T. Heine, R. Banerjee, Solid state organic amine detection in a photochromic porous metal organic framework, *Chem. Sci.* 6 (2015) 1420–1425.
- [41] Y.-X. Xie, W.-N. Zhao, G.-C. Li, P.-F. Liu, L. Han, A naphthalenediimide-based metal–organic framework and thin film exhibiting photochromic and electrochromic properties, *Inorg. Chem.* 55 (2015) 549–551.
- [42] B. Garai, A. Mallick, R. Banerjee, Photochromic metal–organic frameworks for inkless and erasable printing, *Chem. Sci.* 7 (2016) 2195–2200.
- [43] J.-Z. Liao, C. Wu, X.-Y. Wu, S.-Q. Deng, C.-Z. Lu, Exceptional photosensitivity of a polyoxometalate-based charge-transfer hybrid material, *Chem. Commun.* 52 (2016) 7394–7397.
- [44] S.P. Black, D.M. Wood, F.B. Schwarz, T.K. Ronson, J.J. Holstein, A.R. Stefankiewicz, C.A. Schalley, J.K. Sanders, J.R. Nitschke, Catenation and encapsulation induce distinct reconstitutions within a dynamic library of mixed-ligand Zn₄L₆ cages, *Chem. Sci.* 7 (2016) 2614–2620.
- [45] Z. Jiang, J. Liu, M. Gao, X. Fan, L. Zhang, J. Zhang, Assembling polyoxo-titanium clusters and CdS nanoparticles to a porous matrix for efficient and tunable H₂-evolution activities with visible light, *Adv. Mater.* 29 (2017).
- [46] G.M. Sheldrick, Crystal structure refinement with SHELXL, *Acta Crystallogr. Sect. C* 71 (2015) 3–8.
- [47] A.L. Spek, SQUEEZE, PLATON a tool for the calculation of the disordered solvent contribution to the calculated structure factors, *Acta Cryst. C* 71 (2015) 9–18.
- [48] A.D. Becke, Becke's three parameter hybrid method using the LYP correlation functional, *J. Chem. Phys.* 98 (1993) 5648–5652.
- [49] J.M. Crowley, J. Tahir-Kheli, W.A. Goddard III, Resolution of the band gap prediction problem for materials design, *J. Phys. Chem. Lett.* 7 (2016) 1198–1203.
- [50] W.-X. Zhang, W. Xue, X.-M. Chen, Flexible mixed-spin kagome coordination polymers with reversible magnetism triggered by dehydration and rehydration, *Inorg. Chem.* 50 (2011) 309–316.
- [51] F. Pointillart, C. Train, M. Gruselle, F. Villain, H.W. Schmalz, D. Talbot, P. Gredin, S. Decurtins, M. Verdaguier, Chiral templating activity of tris(bipyridine)ruthenium (II) cation in the design of three-dimensional (3D) optically active oxalate-bridged $\{[\text{Ru}(\text{bpy})_3][\text{Cu}_{2-x}\text{Ni}_{2(1-x)}(\text{C}_2\text{O}_4)_3]\}_n$ ($0 \leq x \leq 1$; bpy = 2, 2'-bipyridine): structural, optical, and magnetic studies, *Chem. Mater.* 16 (2004) 832–841.
- [52] L. Wang, W. Yang, Y. Li, Z. Xie, W. Zhu, Z.-M. Sun, Dynamically controlled one-pot synthesis of heterogeneous core–shell MOF single crystals using guest molecules, *Chem. Commun.* 50 (2014) 11653–11656.

- [53] C.L. Whittington, L. Wojtas, R.W. Larsen, Ruthenium(II) tris(2,2'-bipyridine)-templated zinc(II) 1,3,5-tris(4-carboxyphenyl)benzene metal organic frameworks: structural characterization and photophysical properties, *Inorg. Chem.* 53 (2014) 160–166.
- [54] C.L. Whittington, L. Wojtas, W.-Y. Gao, S. Ma, R.W. Larsen, A new photoactive Ru(II)tris(2,2'-bipyridine) templated Zn(II) benzene-1,4-dicarboxylate metal organic framework: structure and photophysical properties, *Dalton Trans.* 44 (2015) 5331–5337.
- [55] H. Xu, J. Gao, J. Wang, X. Qian, R. Song, Y. Cui, Y. Yang, G. Qian, Surfactant-thermal method to synthesize a new Zn(II)-trimesic MOF with confined Ru(bpy)₃²⁺ complex, *J. Solid State Chem.* 226 (2015) 295–298.
- [56] T.F. Willems, C.H. Rycroft, M. Kazi, J.C. Meza, M. Haranczyk, Algorithms and tools for high-throughput geometry-based analysis of crystalline porous materials, *Microporous Mesoporous Mat.* 149 (2012) 134–141.
- [57] C. Wang, M. Zheng, W. Lin, Asymmetric catalysis with chiral porous metal–organic frameworks: critical issues, *J. Phys. Chem. Lett.* 2 (2011) 1701–1709.